Journal of Magnetism and Magnetic Materials 484 (2019) 164–171

Contents lists available at ScienceDirect

Journal of Magnetism and Magnetic Materials

journal homepage: www.elsevier.com/locate/jmmm

Research articles

Interpretation of signature waveform characteristics for magnetic anomaly detection using tunneling magnetoresistive sensor☆

Ying Shen[a,b,c], Jiazeng Wang[a,b,c], Jiedong Shi[a,b,c], Shuxiang Zhao[a,b,c], Junqi Gao[a,b,c,*]

[a] Acoustic Science and Technology Laboratory, Harbin Engineering University, Harbin 150001, China
[b] Key Laboratory of Marine Information Acquisition and Security (Harbin Engineering University), Ministry of Industry and Information Technology, Harbin 150001, China
[c] College of Underwater Acoustic Engineering, Harbin Engineering University, Harbin 150001, China

ARTICLE INFO

Keywords:
Magnetic signature
Waveform characteristics
Magnetic anomaly detection
Tunneling magnetoresistive sensor

ABSTRACT

A detection procedure by employing the induced magnetic signature characteristics for magnetic targets detection and identification is proposed in this paper. The highly sensitive tunneling magnetoresistive (TMR) sensor with low self-noise is adopted, while the magnetic target is traveling along a straight line at various speed and CPA (closest path approach) for magnetic anomaly detection (MAD). The triple-axis TMR sensor is characterized with a high sensitivity around 100 mV/V/Oe in a linear range of ± 1 Oe and a self-noise of 170 pT/√Hz at 1 Hz. The signature waveform width and sensing range angle are used to analyze the signatures. It is found that the sensing range angle is independent of changing velocity and CPA. The proposed signature interpretation strategy is demonstrated by both experimental and simulated data.

1. Introduction

As a result of magnetization by the Earth's magnetic field, a metallic material can create distortions in the local geomagnetic field along each of its three orthogonal directions. Magnetic anomaly detection (MAD) is the use of such phenomenon by magnetic sensors because of the passage of a metallic material nearby a stationary sensor or when a sensor is mounted on a moving platform to sense a stationary target. The MAD method has been proven to work aboard in traffic surveillance [1,2], vehicle parking [3], sea mine hunting [4–6], security checking [7], unexploded ordnance discrimination [8,9], subsea cable [10] and underwater vehicle detection [11,12].

Estimation of the target location is always a concern during the MAD measurement. As expected, metallic objects manifest themselves as unique voltage signal at the outputs of magnetic sensors or gradiometers. Such quantitative information can be employed to predict the magnetic moment and position of the unknown targets, which contains six scalar unknowns [13–15]. Vector magnetic sensors are largely employed in practices to obtain the three magnetic signature vectors, which can be used in a magnetic dipole algorithm to reconstruct the six quantities [16]. However, the interference of environment noise and manufacture limited magnetometer errors invariably affect the sensed magnetic field constituted on the output voltage of the sensors, producing deviations between the estimated and actual object position [17]. To solve the problem, alternative procedure such as orthonormal basis functions (OBFs) method is proposed based on scalar magnetometers. OBFs method aims to analyze the target signal typical patterns on condition of several assumptions, for example the movement is along a straight line track with a constant velocity [18,19]. However, if prior assumptions do not hold, an analytical expression for the OBFs is difficult to be obtained [20]. Moreover, this approach is solved by complex mathematical processes, which add more complexity and involve heavy calculation load.

Indeed, the merit of MAD signal is determined not only by utilizing magnetic signal values for algorithm calculation, but also by interpreting the magnetic fingerprint waveforms comprehensively to estimate the hidden target behavior [21]. Classic OBFs method has indicated that larger characteristic time values lead to wider target signal [22]. Recent studies have also demonstrated a strong dependence of the shapes of the magnetic signature waveforms and the presence, direction, relative distance, velocity and classification of the targets [23,24]. Accordingly, there is a need to understand the underlying physics between the magnetic signature waveforms properties and the unknown target behavior. Here, we use wavelet width and sensing range angle to

☆ This work was supported in part by the Fundamental Research Funds for the Central Universities under Grant HEUCFG201826 and Grant HEUCFJ180508. And the project was supported by China Shipbuilding Indsutry Group Co., Ltd (KY10500190043).

* Corresponding author at: Acoustic Science and Technology Laboratory, Harbin Engineering University, Harbin 150001, China.
E-mail address: gaojunqi@hrbeu.edu.cn (J. Gao).

https://doi.org/10.1016/j.jmmm.2019.04.016
Received 31 January 2019; Received in revised form 24 February 2019; Accepted 4 April 2019
Available online 05 April 2019
0304-8853/

characterize the time-varying magnetic signature by a vector TMR sensor, and propose a procedure to interpret the magnetic signature profile for magnetic field detection and identification.

2. Method

To better understand and estimate the magnetic anomaly signature caused by a dipole movement, a magnetostatic simulation is performed according to the theory of magnetic dipole model. The induced magnetic field $\vec{B}$ by a dipole with a moment of $\vec{M}$ at some distance $\vec{r}$ is:

$$B(\vec{M},\vec{r}) = \frac{\mu_0}{4\pi}\left[\frac{3(\vec{M}\cdot\vec{r})\vec{r}}{|\vec{r}|^5} - \frac{\vec{M}}{|\vec{r}|^3}\right] \tag{1}$$

where $\mu_0 = 4\pi \times 10^{-7} H/m$ is the free space permeability, $\vec{r} = [x \;\; y \;\; z]^T$ is the position vector of the dipole, and $\vec{M} = [M_x \;\; M_y \;\; M_z]^T$ refers to the magnetic moment vector of the target. Bringing $\vec{M}$ and $\vec{r}$ into equation (1) to result a tensor matrix form as:

$$\begin{bmatrix} B_x \\ B_y \\ B_z \end{bmatrix} = \frac{\mu_0}{4\pi R^5}\begin{bmatrix} 3x^2 - R^2 & 3xy & 3xz \\ 3xy & 3y^2 - R^2 & 3yz \\ 3xz & 3yz & 3z^2 - R^2 \end{bmatrix}\begin{bmatrix} M_x \\ M_y \\ M_z \end{bmatrix} \tag{2}$$

where $R = \sqrt{x^2 + y^2 + z^2}$, and $[B_x \;\; B_y \;\; B_z]^T$ are the three components of $\vec{B}$ field in each orthogonal direction.

Fig. 1 illustrates the configuration of a vector sensor and a moving dipole (denoted as α, β and γ) used in this study. The sensor is assigned at the origin of the orthogonal coordinate system. The x-axis is parallel to the line of target motion, the y-axis is vertical to the line of target motion, and the z-axis is perpendicular to the x-y plane. α, β and γ are the angles between the dipole moment and the x-axis, y-axis and z-axis, respectively. The target position is defined as $\vec{r}_m = [x_m \;\; y_m \;\; z_m]^T$ in such model system. The CPA refers to the minimal distance R_0 between the sensor and target. The intersection of the CPA and the target motion line is called CPA point. It should be stated that v is the target motion velocity and the time origin is chosen at the CPA point. Then the position of the target relative to the sensor can be obtained by:

$$x_m(t) = vt; \quad y_m(t) = R_0; \quad z_m(t) = 0 \tag{3}$$

As the components of magnetic moment can be written as:

$$M_x = \cos\alpha\,|\vec{M}|; \quad M_y = \cos\beta\,|\vec{M}|; \; M_z = \cos\gamma\,|\vec{M}| \tag{4}$$

Combining equation (3) and (4) into (2) can introduce the magnetic anomaly signal projected in each orthogonal direction as:

$$\begin{cases} B_x(t) = A[(2v^2t^2 - R_0^2)\cos\alpha\,|\vec{M}| + 3vtR_0\cos\beta\,|\vec{M}|] \\ B_y(t) = A[3vtR_0\cos\alpha\,|\vec{M}| + (2R_0^2 - v^2t^2)\cos\beta\,|\vec{M}|] \\ B_z(t) = A(-v^2t^2 - R_0^2)\cos\gamma\,|\vec{M}| \end{cases} \tag{5}$$

where

$$A = \frac{\mu_0}{4\pi(v^2t^2 + R_0^2)^{\frac{5}{2}}}$$

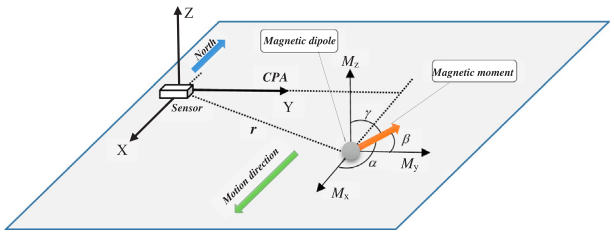

Fig. 1. Scheme illustration of the MAD simulation model.

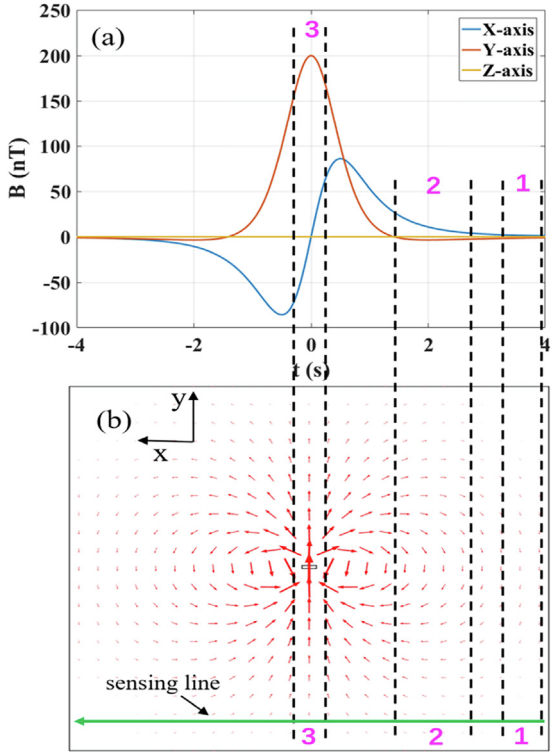

Fig. 2. (a) Typical MAD magnetic signature along three orthogonal directions; (b) Vector map of the x-y component of the H field in the presence of a magnet dipole.

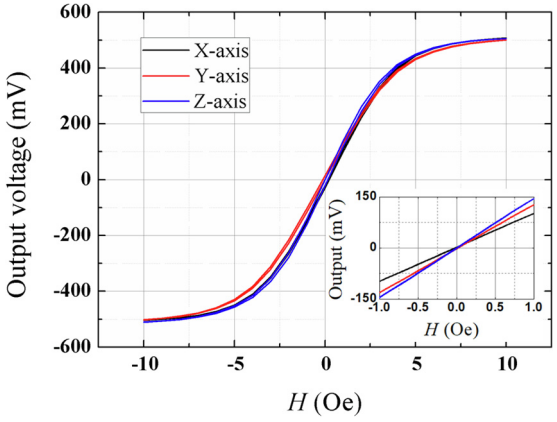

Fig. 3. Transfer curves of sensor output voltage as a function of applied magnetic field in a saturation range of $H = \pm 10$ Oe of the used triple-axis TMR sensor. The insect shows the corresponding transfer curves in a linear range of $H = \pm 1$ Oe.

Set $v = 1$ m/s, CPA = 1 m, $|\vec{M}| = 1\ A{\cdot}m^2$, $\alpha = \gamma = 90°$ and $\beta = 0°$, the induced typical magnetic signature along the three orthogonal directions are given in Fig. 2(a) based on function (5). Note that the precisely correlated zero and peak values for B_x and B_y respectively is a unique indicator of the target's position at the CPA point. In particular, the peak and trough of B_x waveform are point-symmetric at the CPA point; while the B_y profile is completely in axial symmetry along CPA. As expected, the constant B_z of null is a reflection that the object's route lies in x-y plane.

A magnetostatic simulation is performed using a finite element model via a Comsol 5.3 AC/DC Module for a magnet. An automatic 19044 points mesh is generated within a control volume with appropriate boundary conditions, located sufficiently far from regions of

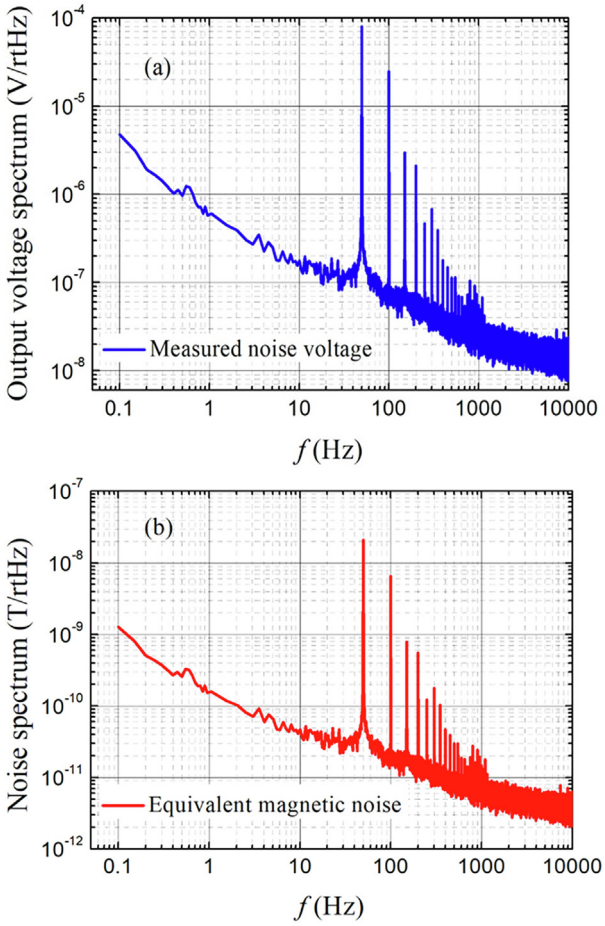

Fig. 4. (a) Voltage noise spectrum of the x-component TMR sensor as a function of frequency from 0.1 Hz to 10 kHz; (b) Equivalent magnetic noise spectrum of the x-component TMR sensor.

interest ambient the dipole. A planar representation of the H field in the space surrounding the magnet is shown in Fig. 2(b). Since the motion is mutual, here a sensor is assigned to be moving along the sensing line from right to left to create a MAD scenario. The magnetic flux geometry in the space close to the sensing line is found to be dramatically influenced by the relative distance between the dipole and sensor.

Comparison of Fig. 2(a) and (b) reveals that both signature waves keep flat at the very beginning when the sensor travels in domain 1 far from the dipole. In domain 2, the B_x curve starts to rise up while B_y one stays null, which are evidenced by the flux density distortion pattern shown in Fig. 2(b). It can be clearly seen that the magnetic flux along x-axis is dominant in domain 2. The magnetic field along y-axis and corresponding flux density B_y begins to be distorted in region 3 (see Fig. 2(a)) of close proximity to the dipole, and reaches a peak where the flux density of B_y is more overwhelming than that of B_x (see Fig. 2(b)). The precisely correlated zero and peak values for B_x and B_y respectively (lying in domain 3) is a unique indicator of the target's position at the CPA point. Since the magnetic flux geometry manner is axisymmetric along the CPA line shown in Fig. 2(b), the B_x is observed to have the same amplitude but opposite direction and B_y experiences a similar decline (see Fig. 2(a)) after passage of the CPA point.

Previous MAD studies have intensively contributed to take B field values from outputs of magnetometers to approach the six unknowns for the target moment and position in equation (1) by various algorithms. In fact, the unique special and temporal signature waveforms shown in Fig. 2(a) embody rich information, which is fundamental to the success in solving the detection problem.

3. Demonstration

3.1. Experimental setup

The system used for the experimental test is based on TMR sensing elements (MultiDimension Technology Co., Ltd, China) and corresponding voltage amplifier circuit, used in conjunction with a non-magnetic slide rail to carry a magnetic target. The triple-axis TMR sensor has a high sensitivity around 100 mV/V/Oe and a self-noise of 170 pT/$\sqrt{}$Hz at 1 Hz. The magnetic field sensitivity is characterized as a

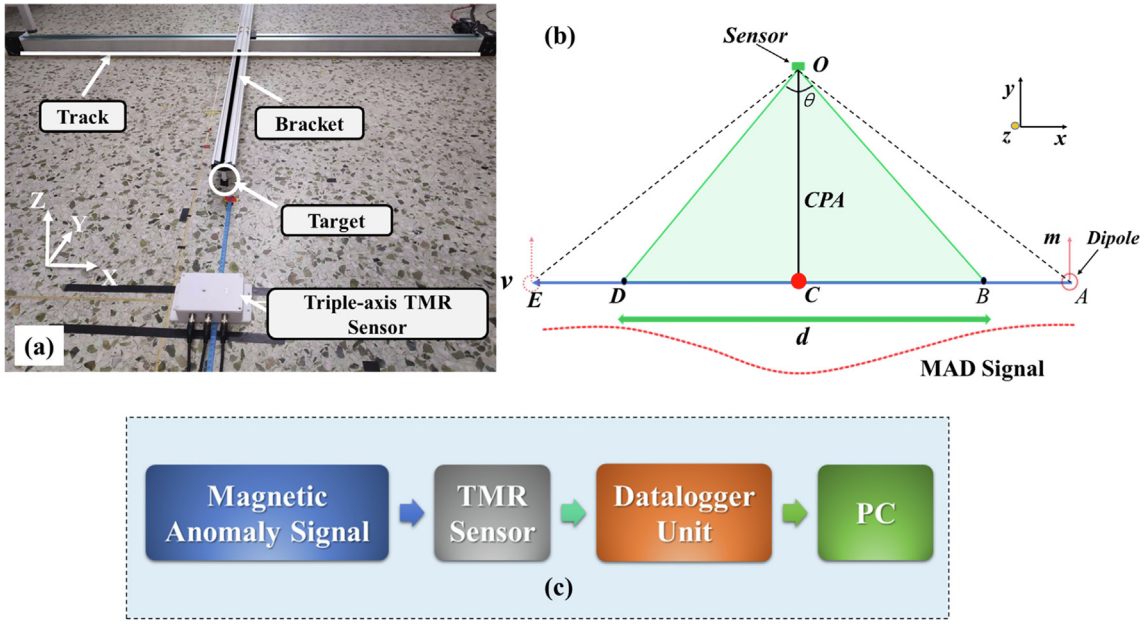

Fig. 5. (a) Experiment setup picture including a 1.85 m slide track, a movable aluminum cantilever and a triple-axis TMR sensor; (b) Scheme illustration of the experiment setup. The CPA is the vertical dimension between the sensor and the moving route line. '*AE*' refers to the 1.85 m long slide track. Distance from point '*B*' to '*D*' is defined as *d*, accounting for the magnetometer's sensing range with respect to the target. The angle between '*B*' and '*D*' is sensing range angle θ; (c) Block diagram of experimental setup.

Table 1
List of experimental setup variables.

	CPA (m)	V (m/s)	Slider range (m)
Velocity effect	0.4	0.2, 0.3, 0.4, 0.5, 0.6, 0.8, 1.0, 1.2	1.85
CPA effect	0.35, 0.4, 0.45, 0.5, 0.55, 0.6, 0.65	0.5	1.85

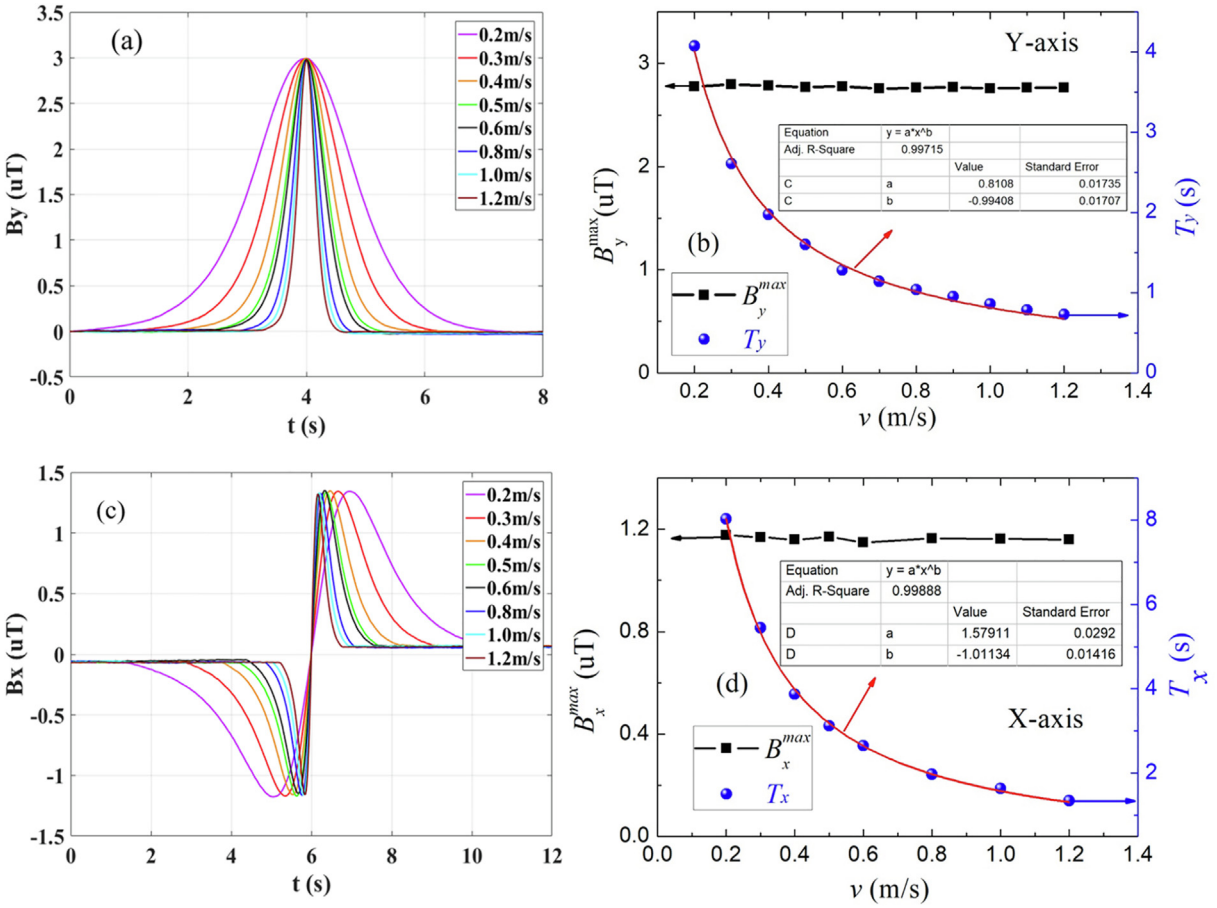

Fig. 6. When keeping CPA constant of 0.4 m with changed v = 0.2, 0.3, 0.4, 0.5, 0.6, 0.8, 1.0, 1.2 m/s respectively, (a) measured magnetic anomaly signal B_y along y-axis in time domain; (b) measured results of B_y^{max} and T_y as a function of velocity; (c) measured magnetic anomaly signal B_x along x-axis in time domain; (d) measured results of B_x^{max} and T_x as a function of velocity.

function of magnetic field (H) in a saturation range of $H = \pm 10$ Oe shown in Fig. 3, where the value of sensitivity is determined by the slope of the transfer curve. The TMR sensor is excited by a 1 V voltage bias; meanwhile, a DC magnetic field is applied along the sensing axis of the sensor using a pair of electromagnets. In a linear range of $H = \pm 1$ Oe shown in the inset of Fig. 3, the sensitivity of 99.20, 125.20 and 143.80 mV/V/Oe are observed for x-, y- and z-axis, respectively.

In a zero-Gauss magnetically shielding chamber, the noise spectrum density for the TMR sensor is measured in a frequency range of $0.1 < f < 10^4$ Hz. A low-noise voltage amplifier (Standford SR560) is employed to enlarge the TMR element noise signal. The SR560 is set at a differential mode to reject the common external noise, and the analogue output signal is sent to a datalogger (USB6210, National Instruments, USA) for data acquisition. The x-component equivalent magnetic noise spectrum shown in Fig. 4(b) is obtained through a conversion of the voltage noise density spectrum (see Fig. 4(a)) using the TMR sensitivity value (see Fig. 3). The equivalent magnetic noise of the x-component TMR sensor is found to be 170 pT/$\sqrt{\text{Hz}}$ at 1 Hz and 1.2 nT/$\sqrt{\text{Hz}}$ at 0.1 Hz. The low equivalent magnetic noise poises such TMR sensor as a viable competitor for opportunities in very sensitive magnetic field magnetometers. The noise spectrum of the other two axes are similar to that of x-axis, which are not shown here.

The experiment setup picture is shown in Fig. 5(a). A small 2 mm thick permanent magnet with 20 mm diameter is used as the target dipole, which is placed on an aluminum cantilever of the slide track. The dipole moment is parallel to y-axis. The cantilever can readily move on the 1.85 m long track from point '*A*' to '*E*' at a controlled velocity, as illustrated in Fig. 5(b). The outputs signal from the triple-axis TMR sensor located at point '*O*' are directly collected by a datalogger (USB6210, National Instruments, USA) with a 100 Hz sample rate and ± 10 V full-scale read-out. The CPA is represented by the vertical dimension between the sensor and the moving route line, and point '*C*' serves as the CPA point. Distance from point '*B*' to '*D*' is defined as d, accounting for the magnetometer's sensing range with respect to the target. In other words, given the presence of sensor's self-noise and environmental noise, '*B*' and '*D*' points refer to the detection limits for the target, and the magnetic signatures should be obtained within the scope of d. In light of Figs. 2 and 5(b), it is understood intuitively that the induced field along x-axis B_x should have larger d than that of B_y. And the angle between '*B*' and '*D*' is termed as sensing range angle θ. The analysis of d and θ for the magnetic signature interpretation are

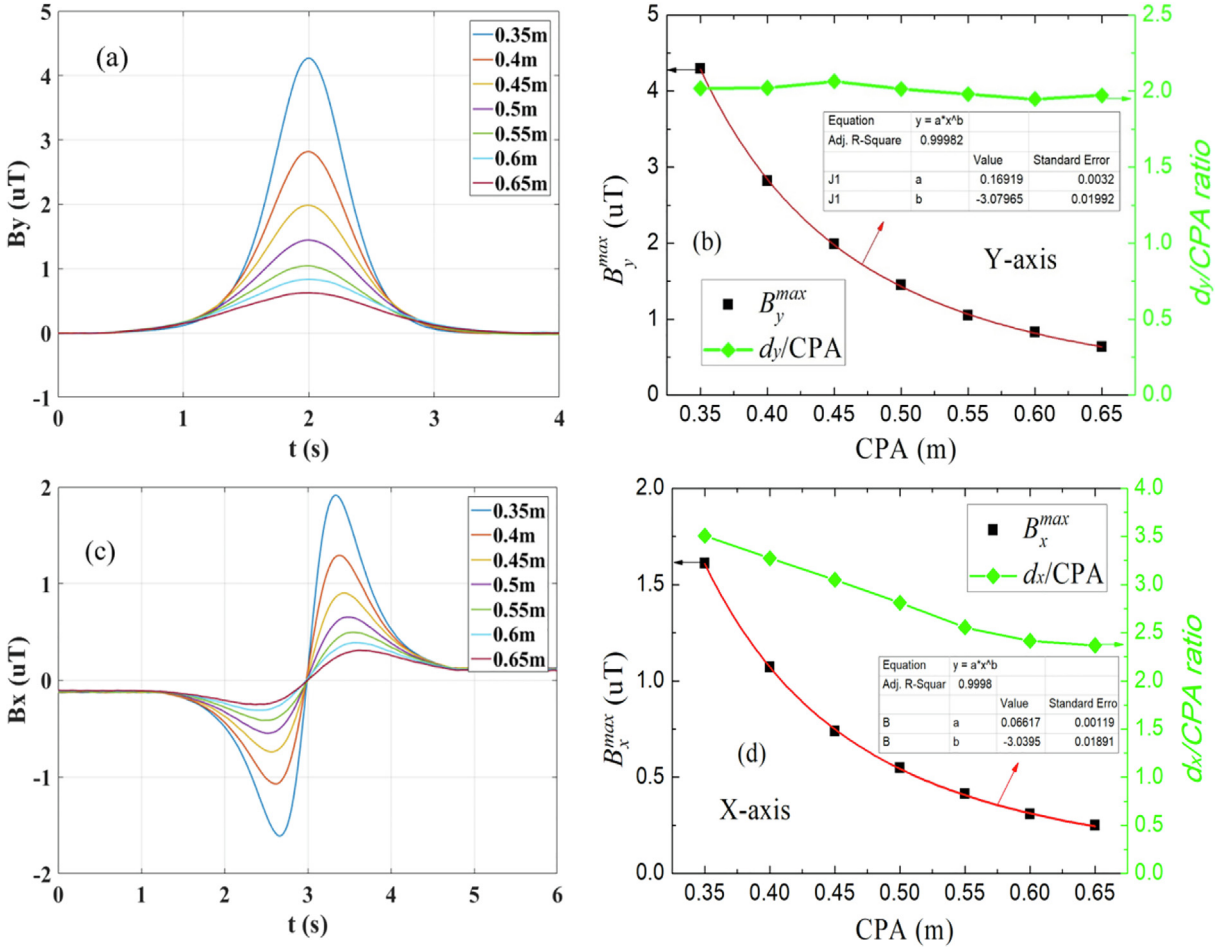

Fig. 7. When keep velocity constant with changed CPA = 0.35, 0.4, 0.45, 0.5, 0.55, 0.6, 0.65 m, respectively, (a) measured magnetic anomaly signal B_y along y-axis in time domain; (b) measured signature peak strength B_y^{max} and d_y/CPA ratio as a function of CPA; (c) measured magnetic anomaly signal B_x along x-axis in time domain; (d) measured results of B_x^{max} and d_x/CPA ratio as a function of CPA.

exemplified in the following experiment and simulation sections. The block diagram of experimental setup is shown in Fig. 5(c). The MAD signal created by moving magnet is detected by a TMR sensor nearby, then the data acquisition is carried out by the datalogger unit.

3.2. Experiment results

The experiment setup variables are given in Table 1. The effect of the target moving velocity is firstly examined at CPA = 0.4 m with v of 0.2, 0.3, 0.4, 0.5, 0.6, 0.8, 1.0 and 1.2 m/s, respectively. Typical time-varying magnetic signature waveforms along y-axis and x-axis are illustrated in Fig. 6(a) and (c), respectively. Since the target experiences a movement in x-y plane, the output signal of z-component is almost none which is not illustrated here. In Fig. 6(a) and (c), it can be seen that the signature peaks turn into narrower and sharper as v increases, which corresponds well with previous report [23]. Fig. 6(b) and (d) show the induced signature peak strength in the two orthogonal axes (B_y^{max} and B_x^{max}) and the width of the wavelet T as a function of v. T is characterized by the signal width during a 90% drop of the peak value. Please note that B_y^{max} and B_x^{max} have nearly constant amplitudes of 2.78 and 1.17 μT, respectively. The results imply that B^{max} is independent of varying v and only governed by the fixed CPA in this test. Also, as given in Fig. 6(b) and (d), the values of T can be seen to be inversely proportional to v, with a transfer function equal to $vT_y = 0.81$ (y-axis) and $vT_x = 1.58$ (x-axis), respectively. Consequently, they yield constant values of $d_y = 0.81$ m and $d_x = 1.58$ m, respectively. Due to CPA = 0.4 m and waveform symmetry, we find that the sensing range angles θ_y and θ_x are determined to be 90.7° and 126.3° respectively based on pythagorean theorem. Therefore, it is important to find that B^{max}, d and θ are all independent of v. If the target is accelerating, the characteristic of constant θ makes such signature waveforms analysis method promising for the use in real MAD applications.

The effect of CPA is then analyzed with a fixed speed of $v = 0.5$ m/s when CPA = 0.35, 0.4, 0.45, 0.5, 0.55, 0.6 and 0.65 m, respectively. The induced magnetic signature waveforms along y- and x-axis are presented in Fig. 7(a) and (c), respectively. In particular, the peak value decreases fast as CPA increases, whereas the width of the wavelet expands as CPA grows at the same time. Unlike the typical x-axis signature shown in Fig. 2(a), the curves in Fig. 7(c) do not reach the baseline on either side. In the theoretical model (see Fig. 2(a)), the $T \approx 5$ s represents a dipole displacement distance of more than 5 m. In contrast, the limited 1.85 m long slide track only allows the dipole to move in a confined range, which should reside inside of '*BD*'. In consequence, Fig. 7(c) just exhibits partial of the signature waveforms ascribed to the limits of the present experimental facilities. As expected, Fig. 7(b) and (d) show that the peak values (B_y^{max} and B_x^{max}) are inversely proportional to the cube of the CPA, which agree well with the classical magnetic dipole principle shown in equation (1). The sensing range d is then obtained by incorporating $v = 0.5$ m/s and measured T values (shown in Fig. 7(a) and (c)) into equation $d = vT$, and the results of d/CPA ratio for y- and x-axis are also shown in Fig. 7(b) and (d), respectively. According to Fig. 7(b), it should be noted that the d_y/CPA ratio looks constant around 2. It implies that the sensing range angle θ_y keeps stable of 90°, which is immune to the changing CPA. These results

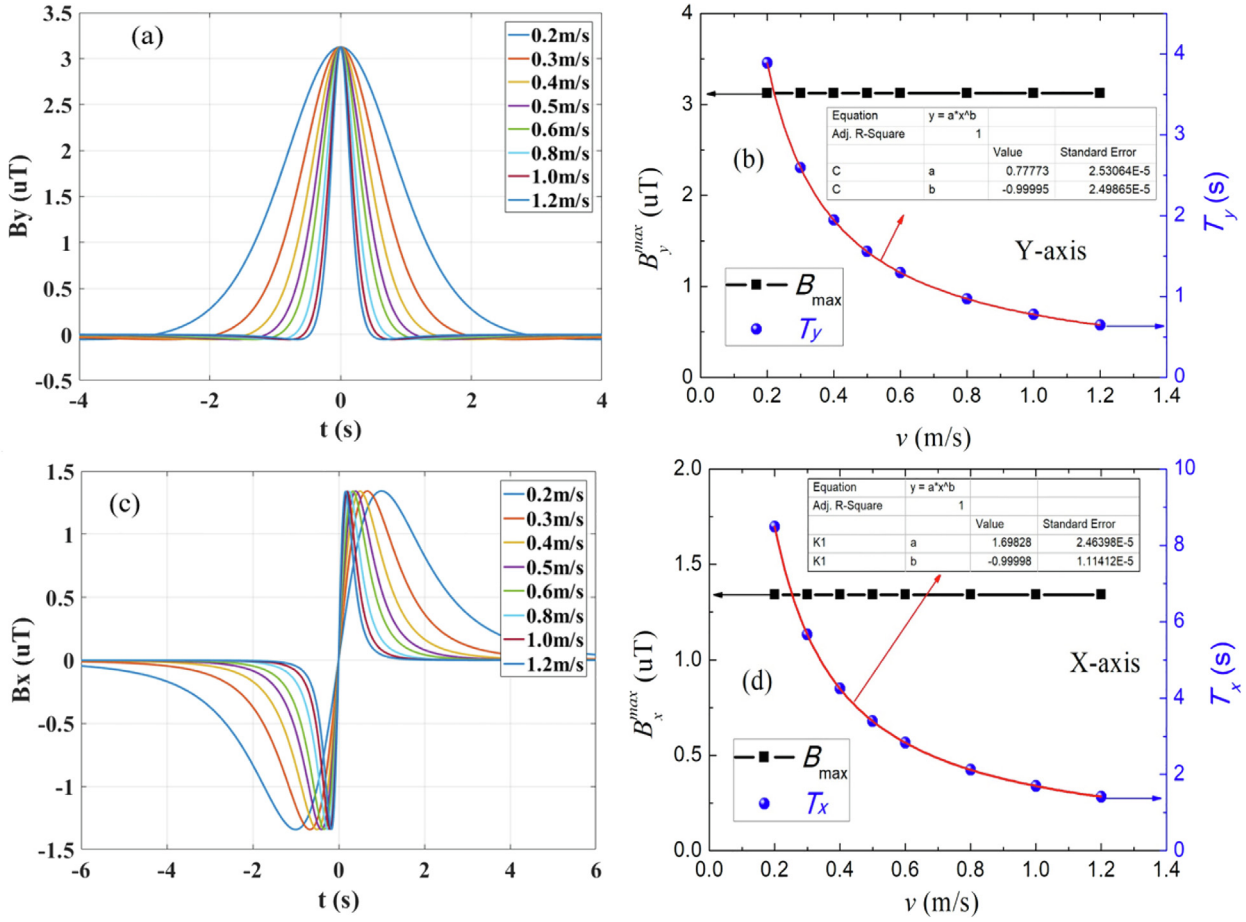

Fig. 8. When keeping CPA constant of 0.4 m with changed v = 0.2, 0.3, 0.4, 0.5, 0.6, 0.8, 1.0, 1.2 m/s respectively, (a) simulated magnetic anomaly signal B_y along y-axis in time domain; (b) simulated results of B_y^{max} and T_y as a function of velocity; (c) simulated magnetic anomaly signal B_x along x-axis in time domain; (d) simulated results of B_x^{max} and T_x as a function of velocity.

show that θ_y is notably independent of v and CPA, and the steady value of $\theta_y = 90^\circ$ may be significant characteristics to estimate the key factors of the target behavior, such as velocity and CPA, based on obtained magnetic signature waveforms. In contract, since the measured d_x values are smaller than that of actual situation, Fig. 7(d) does not present the linear d_x/CPA ratio as a function of CPA. Furthermore, the experimental error escalates as CPA increases, which is demonstrated by the declining d_x/CPA ratio shown in Fig. 7(d).

3.3. Simulation results

Owing to equation (5), the dipole-induced magnetic perturbation is computed on condition that $|\vec{M}| = 1\ A{\cdot}m^2$, angle $\alpha = \gamma = 90^\circ$ and $\beta = 0^\circ$. Fig. 8(a) and (c) shows the simulated time-variable magnetic signature at CPA = 0.4 m along y-axis and x-axis, respectively. Fig. 8(b) and (d) present the corresponding signature peak strength B^{max} and the wavelet width T as a function of v along y-axis and x-axis, respectively. Fig. 8(b) shows that the value of B_y^{max} is stable of 3.13 μT, and T_y is in inverse proportion to v with a transfer function of $vT_y = 0.78$. It suggests that half of the sensing range d_y is 0.39 m (refers to scale of CD or CB) and the angle is equal to $\theta_y = 88.5^\circ$ owing to CPA = 0.4 m, which is close to that of 90.7° in experiment. As shown in Fig. 8(d), T_x is equally inversely proportional to v with a transfer function of $vT_x = 1.70$, producing θ_x to be 129.6°. Comparison of θ values resulted from Fig. 8 and Fig. 6 reveals good agreement between measured ($\theta_y = 90.7^\circ$, $\theta_x = 126.3^\circ$) and predicted ($\theta_y = 88.5^\circ$, $\theta_x = 129.6^\circ$) data. Some variance between the measured and predicted B^{max} and θ values may be due to the magnetic moment value, which is assumed to be 1 $A{\cdot}m^2$ in simulation but it is not precisely the case. The simulation results demonstrate again that the target's velocity affects the time rate of change in the magnetic field perturbations detected by the sensor, thus resulting in different waveform shapes in the signatures. Furthermore, for a given CPA, the d (or θ) value is always a constant parameter determined by vT. Therefore, it is feasible to use the d (or θ) value to estimate the unknown target speed by extracting information of T from the signature waveforms.

The CPA effect is also examined in simulation by changing CPA while keeping other parameters fixed with $v = 0.5$ m/s, $|\vec{M}| = 1\ A{\cdot}m^2$, angle $\alpha = \gamma = 90^\circ$ and $\beta = 0^\circ$. Fig. 9(a) and (c) present the simulated magnetic signature in time-history along the two orthogonal directions. From both figures, we can see that the peak strengths decay fast as CPA rises from 0.35 to 0.65 m. It can also be seen that the waveform widths increase with growing CPA which are in accordance with measured data (see Fig. 7(a) and (c)). Fig. 9(b) and (d) show the response between the peak amplitudes and d/CPA factors as a function of CPA in a manner very close to the test results (see Fig. 7(b) and (d)). In particular, the steady state values of d_y/CPA ratio = 1.94 and d_x/CPA ratio = 4.24 are reflections that the constant sensing range angles of $\theta_y = 88.2^\circ$ and $\theta_x = 129.5^\circ$ respectively. While the simulation has not been configured to allow for accurate determination of the absolute values of the dominating signature characteristics, we believe that the relative d/CPA ratio is physically correct, and supportive of the experimental results to be shown above. These simulation and experiment results together demonstrate that θ_y and θ_x are constant angles independent of changing CPA. Indeed, with the measured wavelet width T, this leads to a straightforward method to identify unknown CPA

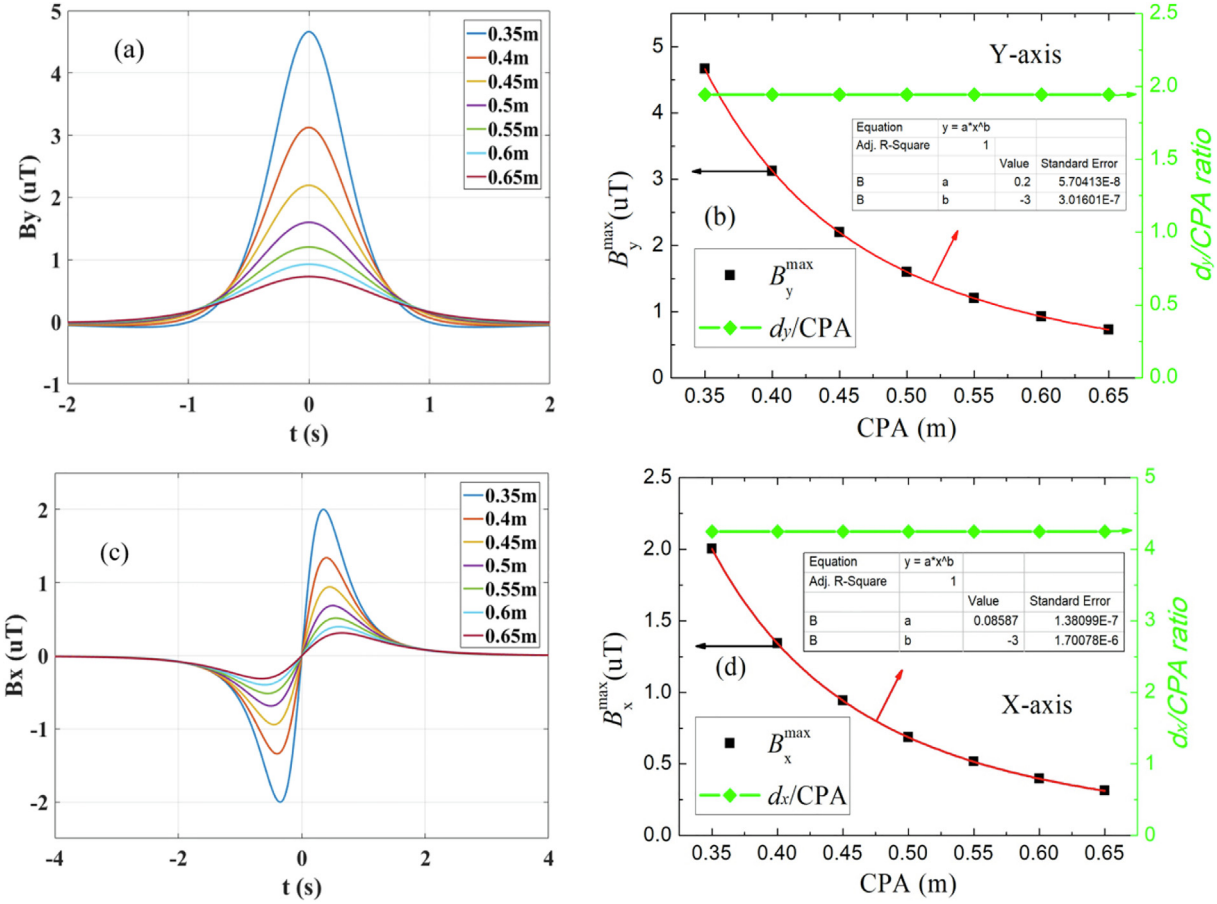

Fig. 9. When keeping $v = 0.5$ m/s with changed CPA = 0.35, 0.4, 0.45, 0.5, 0.55, 0.6, 0.65 m respectively, (a) simulated magnetic anomaly signal B_y along y-axis in time domain; (b) simulated results of B_y^{max} and d_y/CPA ratio as a function of CPA; (c) Simulated magnetic anomaly signal B_x along x-axis in time domain; (d) Simulated results of B_x^{max} and d_x/CPA ratio as a function of CPA.

values based on fixed θ.

4. Conclusion

In summary, a typical dipole induced magnetic anomaly signatures are investigated by a vector TMR sensor with respect to two dependent parameters v and CPA. The signature waveform width T is used as a cue, which has been found to be inversely proportional to the speed with a transfer function of $d = vT$. This has been recognized by previous studies that characteristic time governs the width of the target signal [22], but few quantitative analyses are available. Furthermore, our investigation provides direct evidence that the sensing range angle θ retains to be nearly $\theta_y = 90^\circ$ and $\theta_x = 130^\circ$ for y-axis and x-axis respectively, originating from constant d/CPA factors when the dipole moment is parallel to the y-axis direction. Such merit of stable θ values is important, which can be readily employed to predict the relative distance and velocity of the target. This give us a method attractive for real-time applications such as intruder detection [7,25] and monitoring of the intelligent transportation system [1]. The obtained property in magnetic signatures offers robust and less time-consuming detection procedures that are vital for successful real-time data processing.

Despite the consensus about the feasibility of MAD schemes, they are rarely implemented. More sophisticated procedures for signal whiting, SNR improving, noise suppression, signal processing and signature interpretation, remain confined to research field. One reason for this poor implementation status is the lack of adequate detection, in terms of simple implementation and in-site processing. Thus, implementation of MAD schemes requires a pervasive approach of high detection probability, together with simple realization and low power consumption. Therefore, from a practical point of view, relying on the interpretation of signature waveforms for detection is found to be very efficient for many applications, eliminating the need for a more complicated parallel detection schemes. It is intuitional and quantitative, so that it can be used to trigger a more profound inquiry, which may include information for target localization and magnetic moment estimation. Accordingly, our investigation demonstrates the feasibility of using waveform width T and sensing range angle θ, which is the first step to the interpretation of magnetic fingerprint characteristics. Further works will be devoted to analyze and characterize the relation of θ values and different orientations of the dipoles with changes in α, β and γ targeting real-world applications.

Appendix A. Supplementary data

Supplementary data to this article can be found online at https://doi.org/10.1016/j.jmmm.2019.04.016.

References

[1] A. Haoui, R. Kavaler, P. Varaiya, Wireless magnetic sensors for traffic surveillance, Transp. Res. Part C: Emerg. Technol. 16 (2008) 294–306.
[2] Y. Shen, J. Gao, D. Hasanyan, Y. Wang, M. Li, J. Li, et al., Investigation of vehicle induced magnetic anomaly by triple-axis magnetoelectric sensors, Smart Mater. Struct. 21 (2012) 115007.
[3] Joerg Wolff, T. Heuer, H. Gao, M. Weinmann, S. Voit, U. Hartmann, Parking monitor system based on magnetic field sensors, IEEE Intelligent Transportation Systems Conference, Toronto, Canada, 2006, p. 5.
[4] Y. Ege, S. Nazlibilek, A. Kakilli, H. Çıtak, O. Kalender, K.L. Erturk, et al., A magnetic measurement system and identification method for buried magnetic materials within wet and dry soil, IEEE Trans. Geosci. Remote Sens. 54 (2016) 9.

[5] S. Nazlibilek, O. Kalender, Y. Ege, Mine identification and classification by mobile sensor network using magnetic anomaly, IEEE Trans. Instrum. Meas. 60 (2011) 9.
[6] S. Nazlibilek, Y. Ege, O. Kalender, M.G. Sensoy, D. Karacor, M.H. Sazlı, Identification of materials with magnetic characteristics by neural networks, Measurement 45 (2012) 734–744.
[7] Z. Chu, W. Shi, H. Shi, Q. Chen, L. Wang, C.X. Mohammad Javad PourhosseiniAsl, et al., A 1D magnetoelectric sensor array for magnetic sketching, Adv. Mater. Technol. (2018) 9.
[8] S.D. Billings, Discrimination and classification of buried unexploded ordnance using magnetometry, IEEE Trans. Geosci. Remote Sens. 42 (2004) 11.
[9] V. Sanchez, Y. Li, M.N. Nabighian, D.L. Wright, Numerical modeling of higher order magnetic moments in UXO discrimination, IEEE Trans. Geosci. Remote Sens. 46 (2008) 16.
[10] Z.-Y. Guo, De-Jun Liu, Qi Pan, Y.-Y. Zhang, Forward modeling of total magnetic anomaly over a pseudo-2D underground ferromagnetic pipeline, J. Appl. Geophys. 113 (2015) 17.
[11] J. Zhou, J. Chen, Z. Shan, Spatial signature analysis of submarine magnetic anomaly at low altitude, IEEE Trans. Magn. (2017).
[12] Y. Ege, O. Kalender, S. Nazlibilek, Direction finding of moving ferromagnetic objects inside water by magnetic anomaly, Sens. Actuators, A 147 (2008) 52–59.
[13] T. Nara, S. Suzuki, S. Ando1, A closed-form formula for magnetic dipole localization by measurement of its magnetic field and spatial gradients, IEEE Trans. Magn. 42 (2006) 3.
[14] L. Frumkis, B. Ginzburg, N. Salomonski, B.-Z. Kaplan, Optimization of scalar magnetic gradiometer signal processing, Sens. Actuators, A 121 (2005) 88–94.
[15] B. Ginzburg, L. Frumkis, B.-Z. Kaplan, An efficient method for processing scalar magnetic gradiometer signals, Sens. Actuators, A 114 (2004) 73–79.
[16] Y. Shen, K.L. McLaughlin, J. Gao, D. Gray, L. Shen, Y. Wang, et al., AC magnetic dipole localization by a magnetoelectric sensor, Smart Mater. Struct. 21 (2012) 065007.
[17] Y. Gang, Z. Yingtang, L. Zhining, F. Hongbo, R. Guoquan, Detection of ferromagnetic target based on mobile magnetic gradient tensor system, J. Magn. Magn. Mater. 402 (2016) 7.
[18] B. Ginzburg, L. Frumkis, B.-Z. Kaplan, Processing of magnetic scalar gradiometer signals using orthonormalized functions, Sens. Actuators, A 102 (2002) 9.
[19] C.P. Du, M.Y. Xia, S.X. Huang, Z.H. Xu, X. Peng, H. Guo, Detection of a moving magnetic dipole target using multiple scalar magnetometers, IEEE Trans. Geosci. Remote Sens. 14 (2017) 5.
[20] A. Sheinker, M.B. Moldwin, Magnetic anomaly detection (MAD) of ferromagnetic pipelines using principal component analysis (PCA), Meas. Sci. Technol. 27 (2016) 045104.
[21] Y. Ege, M. Gökhan, O. Sensoy, Kalender, S. Nazlibilek, Numerical analysis for remote identification of materials with magnetic characteristics, IEEE Trans. Instrum. Meas. 60 (2011) 13.
[22] A. Sheinker, B. Ginzburg, N. Salomonski, P.A. Dickstein, L. Frumkis, B.-Z. Kaplan, Magnetic anomaly detection using high-order crossing method, IEEE Trans. Geosci. Remote Sens. 50 (2012) 9.
[23] Y. Shen, D. Hasanyan, J. Gao, Y. Wang, J. Li, D. Viehland, A magnetic signature study using magnetoelectric laminate sensors, Smart Mater. Struct. 22 (2013) 095007.
[24] S. Nazlibilek, Y. Ege, O. Kalender, A multi-sensor network for direction finding of moving ferromagnetic objects inside water by magnetic anomaly, Measurement 42 (2009) 1402–1416.
[25] J. Gao, J. Wang, L. Zhang, Q. Yu, Y. Huang, Y. Shen, magnetic signature analysis for smart security system based on TMR magnetic sensor array, IEEE Sens. J. 19 (2019) 7.